



**HAL**  
open science

# Field and numerical determinations of pneumatic flow parameters of unsaturated fractured porous rocks on various scales

Sophie Guillon, Tan M Vu, Eric Pili, P M Adler

► **To cite this version:**

Sophie Guillon, Tan M Vu, Eric Pili, P M Adler. Field and numerical determinations of pneumatic flow parameters of unsaturated fractured porous rocks on various scales. *Water Resources Research*, 2013, 49 (5), pp.2801 - 2811. 10.1002/wrcr.20263 . hal-01483372

**HAL Id: hal-01483372**

**<https://hal.science/hal-01483372>**

Submitted on 21 Aug 2020

**HAL** is a multi-disciplinary open access archive for the deposit and dissemination of scientific research documents, whether they are published or not. The documents may come from teaching and research institutions in France or abroad, or from public or private research centers.

L'archive ouverte pluridisciplinaire **HAL**, est destinée au dépôt et à la diffusion de documents scientifiques de niveau recherche, publiés ou non, émanant des établissements d'enseignement et de recherche français ou étrangers, des laboratoires publics ou privés.

## Field and numerical determinations of pneumatic flow parameters of unsaturated fractured porous rocks on various scales

S. Guillon,<sup>1,2</sup> M. T. Vu,<sup>3</sup> E. Pili,<sup>1,2</sup> and P. M. Adler<sup>3</sup>

Received 6 October 2012; revised 4 April 2013; accepted 11 April 2013; published 28 May 2013.

[1] Air permeability is measured in the fractured crystalline rocks of the Roselend Natural Laboratory (France). Single-hole pneumatic injection tests as well as differential barometric pressure monitoring are conducted on scales ranging from 1 to 50 m, in both shallow and deep boreholes, as well as in an isolated 60 m<sup>3</sup> chamber at 55 m depth. The field experiments are interpreted using numerical simulations in equivalent homogeneous porous media with their real 3-D geometry in order to estimate pneumatic parameters. For pneumatic injection tests, steady-state data first allow to estimate air permeability. Then, pressure recovery after a pneumatic injection test allows to estimate the air-filled porosity. Comparison between the various studied cases clarifies the influence of the boundary conditions on the accuracy of the often used 1-D estimate of air permeability. It also shows that permeabilities correlate slightly with fracture density. In the chamber, a 1 order-of-magnitude difference is found between the air permeabilities obtained from pneumatic injection tests and from differential barometric pressure monitoring. This discrepancy is interpreted as a scale effect resulting from the approximation of the heterogeneous fractured rock by a homogeneous numerical model. The difference between the rock volumes investigated by pneumatic injection tests and by differential barometric pressure monitoring may also play a role. No clear dependence of air permeability on saturation has been found so far.

**Citation:** Guillon, S., M. T. Vu, E. Pili, and P. M. Adler (2013), Field and numerical determinations of pneumatic flow parameters of unsaturated fractured porous rocks on various scales, *Water Resour. Res.*, 49, 2801–2811, doi:10.1002/wrcr.20263.

### 1. Introduction

[2] Gas flow and transport in unsaturated fractured rocks is of high practical and theoretical interest [Berkowitz, 2002]. Unsaturated fractured geological media are ubiquitous and are of great importance in a number of contexts: underground waste storage [Illman and Hughson, 2005], CO<sub>2</sub> sequestration [Oldenburg et al., 2010], compressed-air energy storage [Kim et al., 2012], remediation of contaminated sites [Switzer and Kosson, 2007], or detection of underground nuclear explosions in the framework of the Comprehensive Nuclear-Test-Ban Treaty [Sun and Carrigan, 2012]. On the theoretical side, several conceptual and mathematical models exist to represent flow and transport in fractured porous media or fractured networks [Long et al., 1982; Bogdanov et al., 2003].

[3] This work is part of a research project aiming at the understanding of gas flow and transport in unsaturated fractured rocks [Pili et al., 2008b] through experiments conducted at the Roselend Natural Laboratory. This underground

research laboratory is well documented thanks to many experiments that have been conducted over the years, such as fracture analyses, tracer experiments as well as long-term monitoring of water and air compositions [Pili et al., 2004; Richon et al., 2005; Patriarche et al., 2007; Pili et al., 2008a]. While water permeability has already been determined at the field scale [Patriarche et al., 2007; Pili et al., 2008a], we address here air flow in unsaturated rocks, and the determination of two key pneumatic parameters, air permeability and air-filled porosity. At the Roselend Natural Laboratory, this knowledge will be of particular importance for forthcoming gas tracer experiments.

[4] Different experimental and numerical approaches exist and have been used to estimate air permeability and air-filled porosity in fractured rocks. Pneumatic injection tests were often conducted in boreholes to estimate air permeability on scales ranging from 1 to 20 m [LeCain, 1997; Bossart et al., 2002; Illman, 2004]. For single as well as cross-holes tests, the methods that are used to estimate permeability are the following: steady-state analyses [Kearl et al., 1990; Baehr and Hult, 1991; Jakubick and Franz, 1993; Guzman et al., 1996; LeCain, 1997; Bossart et al., 2002; Illman and Neuman, 2003], type curve analyses [Illman and Neuman, 2000, 2001; Illman, 2005], 3-D numerical inversions with homogeneous or heterogeneous models [Vesselinov et al., 2001a; Vesselinov and Neuman, 2001; Zhou et al., 2003; Ni and Yeh, 2008], and asymptotic analyses [Illman and Tartakovsky, 2005]. Here pneumatic injection tests are conducted in single holes in three settings, having different locations, sizes and geometries.

<sup>1</sup>CEA, DAM, DIF, F-91297, Arpajon, France.

<sup>2</sup>Institut de Physique du Globe de Paris, Sorbonne Paris Cité, Univ Paris Diderot, UMR 7154 CNRS Paris, France.

<sup>3</sup>UPMC Sisyphé, 4 place Jussieu F-75252, Paris Cedex 05 France.

Corresponding author: S. Guillon, CEA, DAM, DIF, DASE/SRCE, Bruyeres le chatel, F-91297 Arpajon, France. (sophie.guillon@cea.fr)

Analyses of steady state as well as pressure recovery are performed using 3-D numerical simulations in an equivalent homogeneous porous medium, in order to estimate both the air permeability and the air-filled porosity. The use of an equivalent porous model gives first estimates of the flow parameters, that can be used for future simulations of gas flow and transport, and that could be refined when necessary using dual continuum or discrete fracture models [Bogdanov *et al.*, 2003].

[5] Differential barometric pressure monitoring is also used to estimate air permeability in boreholes [Ahlers *et al.*, 1999; Neeper, 2002; Unger *et al.*, 2004]. Here, this second method is applied in only one setting, and 3-D numerical simulations in an equivalent porous medium are again used to estimate the pneumatic parameters. This second method can only estimate the ratio of air permeability to air-filled porosity, but this is very valuable as it is easily performed and can reveal temporal variations of this ratio.

[6] Here we propose an integrated study of pneumatic parameters determinations in the field. The values of the two parameters are determined and compared on various scales, and the use of 3-D versus 1-D numerical models to estimate the permeability is discussed. The results obtained with two experimental methods are compared.

[7] This paper is organized as follows. The experimental site and the three locations that are investigated are presented in section 2. Section 3 details the two experimental methods used for field permeability determination. Section 4 is a brief summary of the conceptual model, the equations solved by the code and the numerical inversion of the experimental data. Section 5 presents the experimental and numerical results for the three types of locations. Finally, section 6 discusses the use of a simplified analytical formula, the relationships between permeability and other rocks parameters.

## 2. The Roselend Natural Laboratory

[8] The site is located in the South-East of France, 25 km south-west from Mont Blanc. It belongs to the External Crystalline Massifs of the Western Alps. The Roselend Natural Laboratory is composed of a dead-end horizontal tunnel at an elevation of 1576 m, located below an abandoned quarry. The tunnel is 128 m long and ca. 2.4 m in diameter. It is hosted in fractured gneisses and micaschists and capped with the same rocks with an increasing thickness from 7 m at the entrance to 55 m at its closed end (Figure 1a). The tunnel is located nearby and above the Roselend lake. Head measurements in two piezometers located between the tunnel and the lake indicate that the water table level is approximately 20 m below the tunnel.

[9] At the end of the tunnel, a chamber whose length and volume are 20 m and 60 m<sup>3</sup>, respectively, is isolated by a concrete bulkhead, equipped with a door and connecting plates (Figures 1a and 1d). It is referred to as chamber C. Since Wassermann *et al.* [2011] estimated the thickness of the Excavation Damaged Zone (EDZ) to be approximately 1 m in the tunnel, the bulkhead is anchored by more than 1 m all around the tunnel section (ceiling, walls and floor). The bulkhead is air-tight by design; the door and connecting plates were independently air-proofed in the laboratory at 1600 mbar absolute pressure. A gas tracer experiment was

conducted in chamber C and no direct leakage was observed on the bulkhead, which confirms that it is air-tight.

[10] Five 2 m long horizontal boreholes, drilled in the last 50 m of the tunnel wall (Figure 1b) are used in this study. They are designated by Perm 4 to Perm 8. Ten 10 m deep vertical boreholes, designated by SC1 to SC10, were also drilled at the topographic surface (Figure 1c). They are located 55 m above chamber C. The characteristic dimensions of these three types of tested intervals are summarized in Table 1.

[11] The fracture density in Perm and SC boreholes is obtained by counting the number of fracture traces using a borehole televiewer and visual examination of the cores. They are summarized in Tables 2 and 3. The fracture density in chamber C is 0.3 m<sup>-1</sup> and was obtained by Patriarche *et al.* [2007] from the interpretation of fracture traces on the tunnel wall.

## 3. Experimental Methods

### 3.1. Pneumatic Injection Tests

[12] Pneumatic testing was already used successfully in sedimentary and crystalline rocks, for the characterization of the EDZ around underground excavations [Bossart *et al.*, 2002; Jakubick and Franz, 1993; Wassermann *et al.*, 2011], as well as for other purposes [LeCain, 1997; Cook *et al.*, 2003; Wang *et al.*, 1999; Kim *et al.*, 2012]. The method is based on the measurement and interpretation of the pneumatic response to air injection into (or air extraction out of) the volume of a rock mass. The experimental setup of a pneumatic injection test is described as follows. Using an air compressor (Metabo, Power 150) and a thermal mass flow regulator (Brooks Instruments, SLA 5850), air is injected at a constant rate into the borehole, which is isolated from the atmosphere by an inflatable packer. Pressure in the packed-off volume is monitored with a time step of 5 s using a pressure transducer (Keller, PAA23RY), and a data logger (Fluke, Hydra 2635A). Because of air injection, pressure increases in the borehole. After 5 min to 20 h, pressure reaches a plateau. Then, air injection is stopped and the subsequent pressure decrease is monitored, typically during 2–20 h. When possible, this pneumatic injection test is conducted with at least two air injection rates. This method is used in the horizontal boreholes Perm in the tunnel wall and in the vertical boreholes SC at the topographic surface.

[13] A similar method is used in chamber C, with the air-tight bulkhead playing the role of the packer. Air is injected at constant pressure into the chamber with a blower (ElmoRiechle, G-BH1) equipped with a relief valve adjusted to around 200 mbar overpressure. In this case, the air injection flow rate is not controlled; it is very high during the first minutes and the target pressure is rapidly reached. Then, a small and constant portion of the air flow is injected into chamber C, while the rest simply flows through the check valve back into the tunnel. A volumeter (Gallus, 6/20 SD) monitors the air injection flow rate into chamber C, and a barometric pressure sensor (GE Sensing, RPT 410) monitors pressure in chamber C, using a data logger (Campbell Scientific, CR 1000) and a 15 min time step. The constant overpressure is maintained during 1–60 h. When the blower is turned off, the pressure

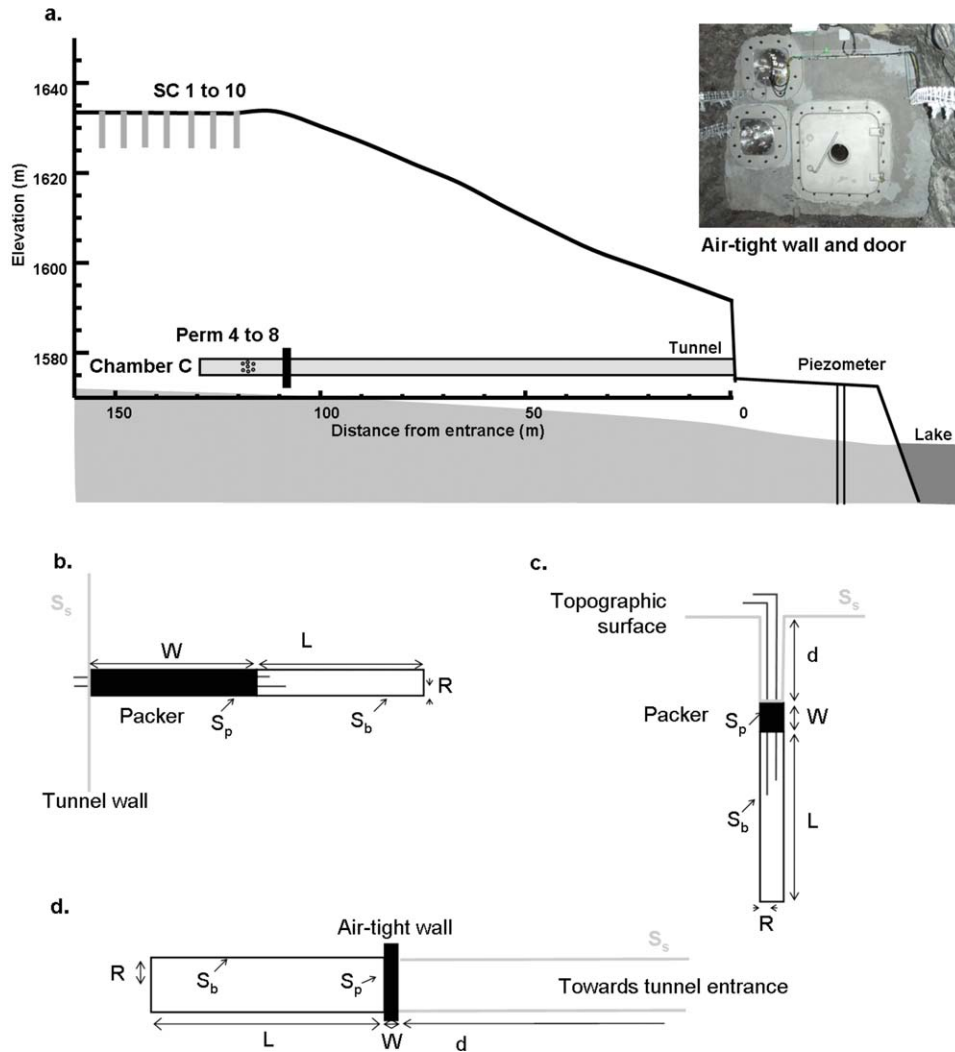


**Figure 1.** The experimental site. (a) Cross section of the Roselend Natural Laboratory with the locations and names of the boreholes and the chamber used in this study; inset: the air-tight bulkhead and door viewed from the chamber. (b) Horizontal boreholes Perm in the tunnel wall. (c) Vertical boreholes SC at the surface. (d) Chamber C at the end of the tunnel.

decrease is monitored. In chamber C, such pneumatic injection tests are repeated several times during 1 year, during both dry and wet periods.

**3.2. Differential Barometric Pressure Monitoring**

[14] Pressure monitoring in boreholes was already used to characterize permeability in the unsaturated zone [Ahlers et al., 1999; Neeper, 2002; Unger et al., 2004; Cook et al., 2003]. This method is applied here to chamber C. Pressure was monitored during more than 3 months in both the chamber and the atmosphere, by two pressure sensors (GE

**Table 1.** Characteristic Dimensions of the Three Types of Tested Intervals

	Packer Depth, $d$ (m)	Packer Length, $W$ (m)	Test Interval Length, $L$ (m)	Radius, $R$ (cm)
Borehole perm	0	1	1.5	4
Borehole SC	3	1	6	5
Chamber C <sup>a</sup>	108	1	20	120

<sup>a</sup>“packer” designates the air-tight bulkhead, and  $d$  corresponds to the distance between this bulkhead and the tunnel entrance.

Sensing, RPT 410) logged on the same data logger (Campbell Scientific, CR 1000) with a 15 min time step.

**4. Numerical Methods**

**4.1. Conceptual Model**

[15] Here, we consider single phase air flow through a homogeneous porous medium with an equivalent air

**Table 2.** Permeability and Porosity Estimated From Pneumatic Injection Tests in the Tunnel Boreholes Perm

Borehole Name	Flow Rate, $M_b$ ( $L \text{ min}^{-1}$ )	Overpressure, $\Delta P$ (mbar)	Permeability, $k$ ( $m^2$ )	Porosity, $\epsilon$ (%)	Fracture Density, ( $m^{-1}$ )
Perm 4	0.1	1450	$6 \times 10^{-17}$	0	0
Perm 5	0.2	200	$1 \times 10^{-15}$	2.7	1.9
Perm 6	0.2	58	$6 \times 10^{-15}$	2.5	0.8
Perm 6	0.8	156	$8 \times 10^{-15}$	3.2	0.8
Perm 7	0.2	71	$4 \times 10^{-15}$	3.3	2.6
Perm 7	0.4	104	$5 \times 10^{-15}$		2.6
Perm 8	0.2	504	$6 \times 10^{-16}$	2.2	0.4

**Table 3.** Permeability Estimated From Pneumatic Injection Tests in the Surface Boreholes SC

Borehole name	Flow Rate, $M_b$ ( $L \cdot \text{min}^{-1}$ )	Overpressure, $\Delta P$ (mbar)	Permeability, $k$ ( $\text{m}^2$ )	Porosity, $\varepsilon$ (%)	Fracture Density, ( $\text{m}^{-1}$ )
SC1	1	536	$7 \times 10^{-16}$	1.5	1.0
SC1	0.2	317	$5 \times 10^{-16}$	1.8	1.0
SC2	0.2	28	$1 \times 10^{-15}$	0.2	1.6
SC3	0.2	18	$1 \times 10^{-16}$	0.5	1.0
SC4	0.2	150	$8 \times 10^{-16}$	3.0	1.1
SC6	5	25	$8 \times 10^{-14}$		1.0
SC7	5	75	$2 \times 10^{-14}$	1.3	1.4
SC7	2	30	$3 \times 10^{-14}$	1.4	1.4
SC9	5	21	$1 \times 10^{-13}$	1.6	2.2
SC9	2	9	$1 \times 10^{-13}$	1.4	2.2
SC10	2	176	$5 \times 10^{-15}$	1.6	2.1
SC10	0.5	85	$4 \times 10^{-15}$	2.5	2.1

permeability  $k$  ( $\text{m}^2$ ) which takes into account the presence of fractures. An important approximation is made by calculating the pressure field and the flow rates using a Darcy equation and replacing the fracture network by a homogeneous porous medium, but such an approximation was justified by *Long et al.* [1982] for large samples, large fracture density and random fracture orientation. Such an approach would be precise when the size of the investigated domain is much larger than the size of the fractures. In this respect, *Patriarche et al.* [2007] showed that the fractures along the Roselend tunnel belong to two families; the first one consists of small fractures with an average diameter of 2.9 m and a random orientation, while the second one consists of large subvertical fractures with an average diameter of 15 m. Here, the three types of experiments can be characterized by the following dimensions: the characteristic lengths of the boreholes Perm, SC, and chamber C are 1.5, 6, and 20 m, respectively (Table 1). Therefore, the continuum approximation is expected to be rough for boreholes Perm, acceptable for boreholes SC and good for chamber C.

[16] A detailed study of the pressure in fracture networks is possible and has already been conducted for different applications by *Mourzenko et al.* [2011]. However, such a study relies on a realistic model of the fracture network for each borehole, taking into account the observed fracture densities (Tables 2 and 3). Such detailed models would most probably lead to permeability estimations with large variations as was observed by *Bogdanov et al.* [2003]. Even for the worst case of boreholes Perm, the permeability estimations obtained in this study are in a narrow range, when the borehole Perm 4, which does not cross any fracture, is omitted. Last, the generation of fracture networks requires a larger number of assumptions than the one of a continuous model where the only unknowns are permeability and porosity. Thus, it was preferable to start with a simple homogeneous model to provide a first estimation of the permeabilities and porosities in all cases.

## 4.2. Governing Equations

[17] Air is assumed to be isothermal and slightly compressible. The air density  $\rho$  ( $\text{kg} \cdot \text{m}^{-3}$ ) is related to the pressure  $P$  (Pa) by

$$\rho = \rho_0 \frac{P}{P_0}, \quad (1)$$

where  $\rho_0$  is the air density at the reference pressure  $P_0$ . Note that the average atmospheric pressure  $P_0$  is equal to 850 hPa for the studied site because of its elevation.

[18] Water is considered as motionless. Water saturation  $S_w$  is only taken into account by a reduction of the air-filled porosity  $\varepsilon$  and/or air permeability  $k$ . The Darcy velocity  $\mathbf{v}$  ( $\text{m} \cdot \text{s}^{-1}$ ) is given by Darcy's law

$$\mathbf{v} = -\frac{k}{\mu} \nabla P, \quad (2)$$

where  $\mu$  ( $\text{Pa} \cdot \text{s}$ ) is the air viscosity. The mass flow rate of air  $q_m$  ( $\text{kg} \cdot \text{m}^{-2} \cdot \text{s}^{-1}$ ) is expressed as

$$q_m = \rho \mathbf{v}. \quad (3)$$

[19] Mass conservation implies

$$\frac{\partial \rho \varepsilon}{\partial t} + \nabla \cdot (\rho \mathbf{v}) = 0. \quad (4)$$

[20] Introduction of equations (1) and (2) into (4) yields

$$\frac{\partial P}{\partial t} - \frac{k}{\mu \varepsilon} \nabla \cdot (P \nabla P) = 0. \quad (5)$$

[21] The diffusivity  $D$  ( $\text{m}^2 \cdot \text{s}^{-1}$ ) is defined as

$$D = \frac{k P_0}{\mu \varepsilon}. \quad (6)$$

[22] Equation (5) can be made dimensionless by introducing a characteristic length scale  $L$  and a pressure scale  $P_0$ . Values for  $L$  in each case are listed in Table 1. Thus, a system of dimensionless variables which are indicated by primes is defined

$$x' = \frac{x}{L} \quad P' = \frac{P}{P_0} \quad t' = \frac{t}{T} \quad T = \frac{L^2}{D}. \quad (7)$$

[23] The characteristic time  $T$  corresponds to diffusion since equation (5) is a diffusion equation. For simplicity, primes are omitted and equation (5) becomes, in dimensionless units,

$$\frac{\partial P}{\partial t} - \nabla \cdot (P \nabla P) = 0, \quad (8)$$

or,

$$\frac{\partial P}{\partial t} = P \nabla^2 P + \nabla P \cdot \nabla P, \quad (9)$$

or,

$$\frac{\partial P}{\partial t} = \frac{1}{2} \nabla^2 P^2. \quad (10)$$

[24] A no flux boundary condition is assumed at  $z = z_b$  corresponding to the water table, 20 m below the tunnel.

The same condition applies on the vertical boundaries, sufficiently far from the boreholes or the chamber. The air-tight bulkhead or the packers are considered as impermeable, and a no-flux condition is applied on their surface  $S_p$ . These boundary conditions are summarized as

$$\mathbf{n} \cdot \nabla P = 0 \quad \text{for } z = z_b \quad \text{and } \mathbf{x} \in S_p, \quad (11)$$

where  $\mathbf{n}$  is the unit normal to the boundaries.

[25] Equation (10) is solved by the finite difference method [Peyret and Taylor, 1985]. The grid spacing  $\Delta$  is equal to 0.02 m for simulations of boreholes Perm and SC;  $\Delta$  is equal to 0.4 m for the larger scale simulations of chamber C.

[26] All the bounding surfaces (ground, water table, borehole, and tunnel walls) are defined by means of the Level Set Method. In this method, the real surface is defined by a distance function based on the usual fixed Cartesian grid. The interface is represented by a polygonal smooth surface at the zero level of this distance function. With this method, tilted surfaces are represented more accurately than with a standard discretization. Moreover, since the boundary conditions are written on the surface itself, the numerical codes are more precise for the same discretization than the standard codes [Sethian and Smerka, 2003].

[27] The iteration method is explicit in time with a time step  $\Delta t$ . A stability analysis can be easily performed in the one-dimensional case [Hirt, 1968] and it implies

$$\frac{\Delta t}{\Delta^2} \leq 2/5. \quad (12)$$

[28] This approximation gives an order of magnitude for  $\Delta t$  in the computations, namely less than 0.01 s for boreholes Perm and SC, and less than 1 s for chamber C.

### 4.3. Interpretation of the Pneumatic Injection Tests

[29] A test consists of three parts. The first period is the rapid transient pressure buildup in response to air injection, and is discarded here as it mainly involves borehole storage effects and would not be easily modeled. In the second part, both pressure and injection flow rate are constant in time. In the third one, injection is stopped and pressure decreases.

[30] First, consider steady-state conditions. When air is injected into a borehole, an equilibrium state is reached after a variable period of time, and the pressure in the borehole and the injection flow rate are constant. Equation (10) is simplified as

$$\nabla^2 P^2 = 0. \quad (13)$$

[31] The boundary conditions are, for all times,

$$P(\mathbf{x}, t) = P_0 \quad \text{for } \mathbf{x} \in S_s, \quad P(\mathbf{x}, t) = P_0 + \Delta P \quad \text{for } \mathbf{x} \in \text{borehole or chamber C}, \quad (14)$$

where  $\Delta P$  is the steady-state overpressure in the borehole or chamber C, and  $S_s$  is the topographic surface and tunnel wall where barometric conditions apply (Figure 1). In this

situation, the mass flow rate  $M_b$  through the packed-off borehole surface  $S_b$  should be equal to the mass flow rate of air  $M_s$  through the surface  $S_s$ ,

$$M_s = M_b \quad \text{at } t = \infty. \quad (15)$$

[32] In equation (13), the pressure field is independent of permeability, and can be calculated for a fixed pressure in the borehole. The mass flow rate  $M_b$  injected through the borehole surface is measured during the experiment. The permeability  $k$  can be deduced from

$$k = \frac{M_b}{\iint_{S_b} -\frac{\rho}{\mu} \nabla P \cdot d\mathbf{s}}. \quad (16)$$

[33] Second, consider unsteady conditions. Equation (10) is solved as explained above in order to calculate the pressure decrease after the end of the injection. The initial condition in the injection zone (borehole or chamber C) is

$$P(\mathbf{x}, t = 0) = P_0 + \Delta P \quad \text{for } \mathbf{x} \in \text{borehole or chamber C}, \quad (17)$$

and the boundary condition on the surface  $S_s$  is, for all times,

$$P(\mathbf{x}, t) = P_0 \quad \text{for } \mathbf{x} \in S_s. \quad (18)$$

[34] In this case, the diffusivity is needed, which is proportional to the ratio of permeability and porosity. The air permeability is estimated from the steady-state experiment as explained previously (equation (16)). The air-filled porosity is obtained by fitting the calculated and experimental pressure evolutions. The chosen value of porosity is the one that minimizes the sum of the square differences between the numerical and experimental data.

### 4.4. Interpretation of Differential Barometric Pressure Monitoring

[35] The atmospheric pressure is measured as a function of time at the Roselend site and is used in equation (8) as the surface boundary condition

$$P(\mathbf{x}, t) = P_{\text{atm}}(t) \quad \text{for } \mathbf{x} \in S_s. \quad (19)$$

[36] The corresponding evolution of the pressure in chamber C is calculated. The diffusivity  $D$  is chosen in order to fit this calculated pressure in chamber C and the experimental data.

## 5. Results

### 5.1. Tunnel Boreholes Perm

[37] Pneumatic injection tests have been conducted in the horizontal boreholes Perm. The air injection rates range from 0.2 to 0.8 L min<sup>-1</sup>. In all the settings and experiments presented here, overpressures are smaller than 500 mbar, and they should not induce any deformation of the medium or fracture opening. A typical pressure evolution during a pneumatic injection test in a tunnel borehole Perm is presented in Figure 2a. In the borehole Perm 6, an air injection

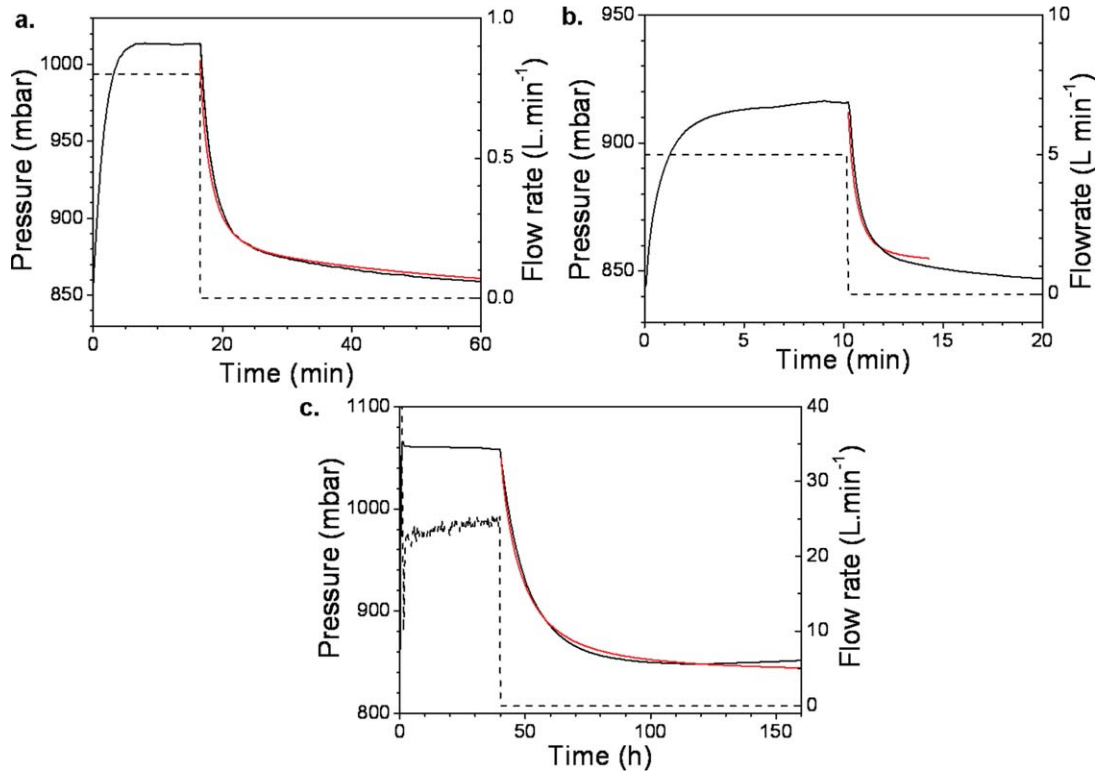


**Figure 2.** Pressure variations (black solid line) and air injection flow rate (dotted line) measured during and after air injections into the three types of tested intervals. The pressure decrease after the end of the injection is reproduced by numerical simulation (red), using the steady-state permeability. (a) Tunnel borehole Perm 6. (b) Surface borehole SC 7. (c) Chamber C (data from 21 September 2011). The experimental parameters and the computed permeabilities are given in Tables 1–4. The sum of the square differences between simulated and measured pressure divided by the number of data points is 8.0 for borehole Perm 6, 3.6 for borehole SC 7 and 28 for chamber C.

flow rate of  $0.8 \text{ L min}^{-1}$  leads to an overpressure of 156 mbar. Pressure increases and reaches steady state after 10 min. At the end of the air injection, pressure decreases to the atmospheric value in less than 1 h. As explained in section 4, the air permeability  $k$  is deduced from the steady-state data (equation (16)).  $k$  is further used to interpret the transient pressure decrease and deduce the porosity.

[38] Figure 3a shows the pressure field and the air streamlines around a tunnel borehole, Perm 6, at steady state. The pressure field is elongated along the borehole axis  $z$ , and pressure decreases rapidly with the distance  $x$  from the borehole. Air flows perpendicular to the borehole axis, but streamlines are bent towards the tunnel wall which is the only atmospheric pressure boundary. As noticed in section 4.1, the smooth pressure field calculated with an equivalent porous model can locally differ from the real pressure field, but the average fracture density is large enough for this approximation to be done.

[39] The computed permeabilities range from  $6 \times 10^{-17}$  to  $8 \times 10^{-15} \text{ m}^2$ , and porosities from 2.2 to 3.3% (Table 2). The 2 orders of magnitude between the permeabilities of boreholes located only 1 m apart reveal the spatial heterogeneity. Since the minimum distance between two boreholes is 1 m and Figure 3a shows that the pressure perturbation is negligible at this distance, interactions between adjacent boreholes are not considered here.

[40] A small increase in permeability with the injection flow rate or overpressure is observed (Table 2). This was also observed by *Illman* [2005], who explained it by the existence of some water flow. At high overpressures, water is displaced by air which increases the local air-filled porosity and air permeability.

## 5.2. Surface Boreholes SC

[41] In the surface boreholes SC, the air injection rates range from  $0.2$  to  $5 \text{ L min}^{-1}$  (Table 3). Figure 2b shows the pressure monitored in the vertical surface borehole SC7 during air injection at  $5 \text{ L min}^{-1}$ . As for tunnel boreholes Perm, the pressure increases and reaches a maximum after about 10 min. Pressure decreases from its steady state value to the atmospheric value in less than 1 h.

[42] The computed permeabilities in boreholes SC range from  $1 \times 10^{-16}$  to  $1 \times 10^{-13} \text{ m}^2$ , and the porosities from 0.2 to 3.0% (Table 3). Permeabilities vary by 3 orders of magnitude over a distance of 20 m. Spatial heterogeneity is strong in the subsurface, as well as for the tunnel boreholes Perm at 55 m depth.

[43] The pressure field and the streamlines around a surface borehole SC are shown in Figure 3b. Results are very similar to those in the tunnel boreholes Perm with a rapid pressure attenuation with distance  $x$  and flow toward the surface which is the atmospheric pressure boundary.

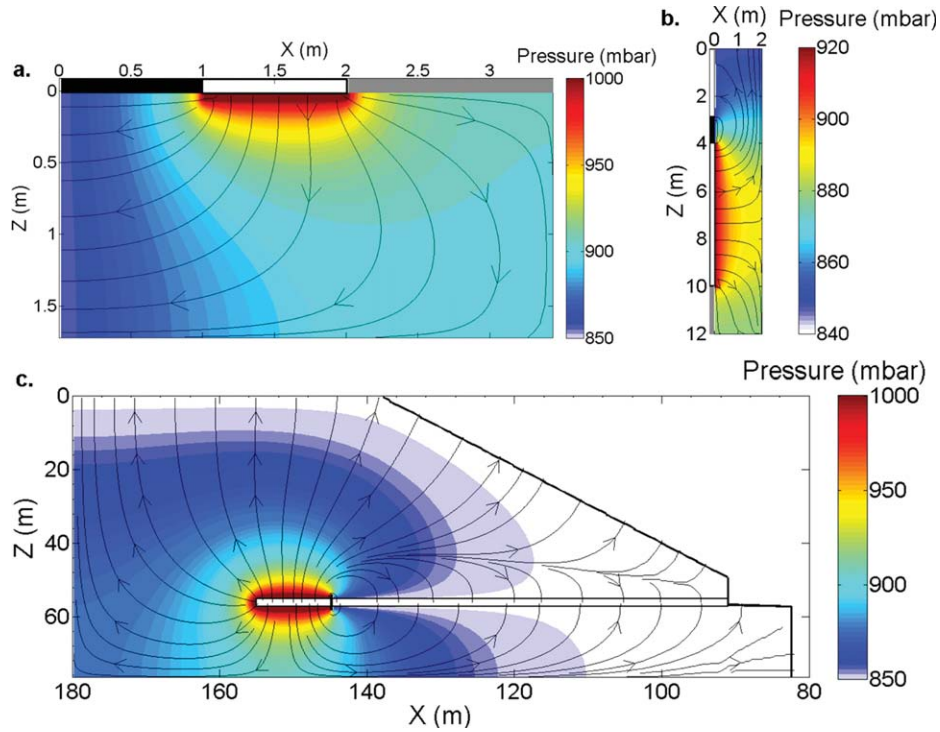


**Figure 3.** 2-D vertical cross sections of 3-D air pressure field and streamlines at steady state during pneumatic injection tests. (a) Tunnel borehole Perm 6. (b) Surface borehole SC 7. (c) Chamber C (same data as in Figure 2).

### 5.3. Chamber C

[44] Figure 2c shows the pressure monitored in chamber C during a pneumatic injection test. As explained in section 3, a constant pressure is imposed during the pneumatic injection tests in chamber C, whereas a constant flow rate is imposed in boreholes Perm and SC. Thus, the pressure evolution in Figure 2c is different from those in Figures 2a and 2b. A flow rate of  $24 \text{ L min}^{-1}$  is needed to maintain an overpressure of 200 mbar in chamber C. Steady state is

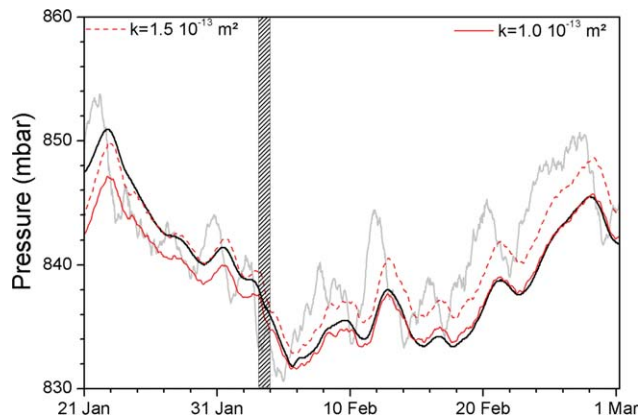


**Figure 4.** Pressure fluctuations measured from January to March 2012, in chamber C (black line) and in the atmosphere (grey line); numerical simulation of pressure in chamber C (red solid and dotted lines) for two values of the permeability  $k$ . The vertical shaded zone separates two successive periods, which are discussed in section 6.3.

reached after a few minutes, even if a small pressure decrease is observed for long injection times (0.2% in 40 h in Figure 2c). After the end of the injection, the pressure decreases during more than 24 h to reach the atmospheric value. The computed permeabilities and porosities for all the successive experiments are in a narrow range (Table 4): the mean and standard deviation for all the tests in chamber C are  $6.4 \pm 1.5 \times 10^{-15} \text{ m}^2$  and  $4.6 \pm 0.07\%$ .

[45] Figure 3c shows the steady-state pressure field and the corresponding streamlines around the chamber during a pneumatic injection test with an overpressure of 200 mbar. Pressure decreases rapidly in a few meters around the chamber. Around 10 m above the tunnel, an imaginary surface can be drawn, that separates an upper zone connected to the topographic surface and a lower zone connected to the tunnel. Only 15% of the air flow is bypassed around the air-tight bulkhead through the tunnel, while 85% of the flow occurs through the topographic surface. This proportion is related to the geometry of the topographic surface and tunnel wall, which are at atmospheric pressure. Such a proportion is not observed in the boreholes SC and in the boreholes Perm, where the surface which is at atmospheric pressure is perpendicular to the injection zone.

[46] Figure 4 shows the pressure fluctuations measured in both the chamber C and the atmosphere. Relatively to the atmospheric pressure, pressure fluctuations in the chamber C are attenuated by a factor between 0.4 and 0.8, with a lag of 24 h. As only the diffusivity can be determined by this method (see section 4), a value is needed for the porosity in order to estimate the permeability. The estimations of the porosity of the rocks at the Roselend Natural Laboratory range from 0.3 to 5% [Richon *et al.*, 2005; Pili *et al.*,

**Table 4.** Permeability and Porosity Estimated From Pneumatic Injection Tests in Chamber C

Date	Flow Rate, $M_b$ (L min <sup>-1</sup> )	Overpressure, $\Delta P$ (mbar)	Permeability, $k$ (m <sup>2</sup> )	Porosity, $\varepsilon$ (%)
14 Sep 2011	23	210	$8 \times 10^{-15}$	4.7
20 Sep 2011	24	213	$8 \times 10^{-15}$	4.6
17 Oct 2011	18	221	$8 \times 10^{-15}$	4.7
14 Jan 2012	18	216	$6 \times 10^{-15}$	4.5
24 Mar 2012	15	202	$5 \times 10^{-15}$	4.6
30 Mar 2012	15	212	$5 \times 10^{-15}$	4.6
6 Apr 2012	15	212	$5 \times 10^{-15}$	4.6

2008a]. In consistence with these estimations and according to the results obtained from pneumatic injection tests in chamber C, the air-filled porosity is supposed to be 5%. A good agreement between the pressure calculated in the chamber and the data are obtained for a permeability of  $1.5 \times 10^{-13}$  m<sup>2</sup>, at least in the first part of the graph from 21 January 2012 until 4 February 2012. From 4 February until 4 March 2012, Figure 4 shows that a better fit is obtained with a permeability of  $1.0 \times 10^{-13}$  m<sup>2</sup>.

[47] Tables 4 and 5 summarize the results for all the pneumatic injection tests and for the differential barometric pressure monitoring periods, respectively.

## 6. Discussion

### 6.1. Analytical Interpretation and Numerical Simulations of Pneumatic Injection Tests

[48] In the approximation of a radial flow around the air injection interval, air permeability is given by [Bossart *et al.*, 2002; Jakubick and Franz, 1993]

$$k = \frac{\mu Z}{\pi L} \frac{T}{T_{std}} q_{ss} \frac{P_{std}}{P_{ss}^2 - P_0^2} \ln\left(\frac{R_e}{R}\right), \quad (20)$$

where  $q_{ss}$  is the air flow rate at steady-state conditions (m<sup>3</sup>·s<sup>-1</sup>),  $P_{ss}$  the pressure in borehole under steady-state conditions (Pa),  $P_{std}$  the pressure under standard conditions (1013.25 hPa),  $P_0$  the average atmospheric pressure (850 hPa),  $T$  the temperature in the borehole or chamber C (283 K),  $T_{std}$  the temperature under standard conditions (298.15 K),  $Z$  the gas deviation factor (0.982),  $\mu$  the air viscosity (1.8110<sup>-5</sup> Pa·s),  $L$  the length of the injection interval (m),  $R$  the borehole radius (m), and  $R_e$  the radius of influence (m). In equation (20),  $R_e$  is the distance from the injection interval to the point at which there is no significant pressure increase due to the pneumatic injection.

[49] In this approach, only steady-state data are used, and the porosity cannot be estimated. The radius of influence is often approximated by the length of the injection interval  $L$  [Freifeld, 2001; Illman, 2004]. Here the pressure field around the injection volume is calculated by 3-D simulations, which provides an insight into the approximation of the radius of influence. According to these simulations, the pressure decreases logarithmically with the radial distance to the injection volume for all three locations. At a distance equal to the injection interval  $L$ , the pressure increase is less than 5%, indicating that this approximation of the radius of influence is acceptable for all cases. For

chamber C, the assumption of radial symmetry is violated, but it appears that the approximation of the radius of influence remains acceptable. Indeed, as the radius of influence only appears as a natural logarithm, it has little influence on the permeability, and the above approximation still applies in most cases.

[50] Permeability was determined with formula (20) for all the pneumatic injection tests, using the parameters in Table 1, and the above approximation for the radius of influence. Results are presented in Figure 5. The differences between the permeabilities estimated in the 1-D approximation and those estimated from numerical simulations in 3-D geometry range from -54 to 200%, with an average absolute difference of 30%. Even though the simplified analytical formula (20) gives permeabilities that are at first order correct, numerical simulations with the real 3-D geometry allow to obtain values for both permeability and porosity, with reduced uncertainty, whatever the geometry of the injection interval and the boundary conditions.

### 6.2. Influence of Fracture Density on Permeability

[51] In surface boreholes SC as well as tunnel boreholes Perm, permeability varies from one borehole to another, with up to 3 orders of magnitude difference in permeabilities estimated in nearby boreholes (Tables 2 and 3). The borehole Perm 4 is characterized by an absence of fracture trace and is associated with the lowest permeability value of  $10^{-17}$  m<sup>2</sup>. Thus, it probably corresponds to the matrix permeability. For scales from 1 to 10 m, this spatial variability is related to the heterogeneity of the fracture network. Figure 6, which gathers all observed data, shows a weak positive correlation between the logarithm of the gas permeability and the fracture density. Close to the surface, permeability and fracture density are on average higher than at depth.

### 6.3. Variability of the Permeability Measured in Chamber C With Various Methods and Role of Water Saturation

[52] In chamber C, air diffusivity obtained from differential barometric pressure monitoring is one order of magnitude higher than air diffusivity obtained from pneumatic injection tests (Tables 4 and 5). This could result either from an increase in air permeability, or a decrease in air-filled porosity, or more probably from a combination of both.

[53] A variation of water saturation cannot explain the discrepancy between the permeability values obtained from the two methods, as the expected behavior is opposite. Indeed, the sometimes observed increase in permeability with the overpressure (Tables 2 and 3) suggests that water can be displaced by the injected air during pneumatic injection tests. By contrast, during differential barometric

**Table 5.** Permeability Estimated From Differential Barometric Pressure Monitoring in Chamber C, with 5% Porosity

Date	Permeability, $k$ (m <sup>2</sup> )
2 Jul to 18 Jul 2011	$1.5 \times 10^{-13}$
6 Aug to 11 Sep 2011	$1.5 \times 10^{-13}$
21 Jan to 4 Feb 2012	$1.5 \times 10^{-13}$
4 Feb to 4 Mar 2012	$1.0 \times 10^{-13}$

pressure monitoring, the medium is only submitted to small natural pressure variations, and water saturation is expected to remain constant. If such variations of water saturation were to exist, the air permeability obtained from pneumatic injection tests should be the higher value, and this is not observed here.

[54] The discrepancy between the air permeability values obtained with two different methods from one single tested interval can be interpreted as a scale effect due to the difference of the sizes of the rock volume actually investigated [Hinds *et al.*, 2003]. Pneumatic injection tests in chamber C would give a permeability that is representative of the volume of rock surrounding the chamber, the size of which is related to the length of the chamber. The permeability estimated from differential barometric pressure monitoring integrates a larger rock volume up to the surface. For crystalline rocks [Brace, 1984; Clauser, 1992] as well as for other rock types [Neuman, 1994; Vesselinov *et al.*, 2001b; Hyun *et al.*, 2002; Illman, 2004, 2006], it has been shown that permeability increases with scale. The permeability estimated from differential barometric pressure monitoring is thus expected to be higher than the permeability estimated from pneumatic injection test in the same tested interval. Vesselinov *et al.* [2001b] proposed that this scale effect is an artifact, caused by the use of a homogeneous model as an approximation of a heterogeneous fractured medium. This scale effect would be suppressed by treating the modeled region as heterogeneous.

[55] The use of a single-phase flow model is another limitation that could partly explain the apparent contradiction between the two experimental methods. Numerical simulations of two-phase flow would give insights into the influence of pneumatic injection tests on saturation and water movements. Such a relation between air permeability and variations of water saturation could be observed with differential barometric pressure monitoring. In Figure 4, a

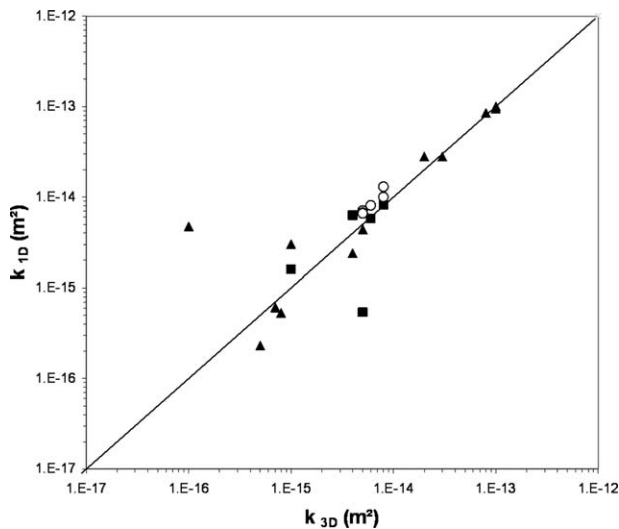


**Figure 5.** Permeability determined from steady-state data using equation (20) for a 1-D radial model versus permeability determined from numerical simulations in the real 3-D geometry. Data are for pneumatic injection tests in tunnel boreholes Perm (squares), surface boreholes SC (triangles), and chamber C (circles).

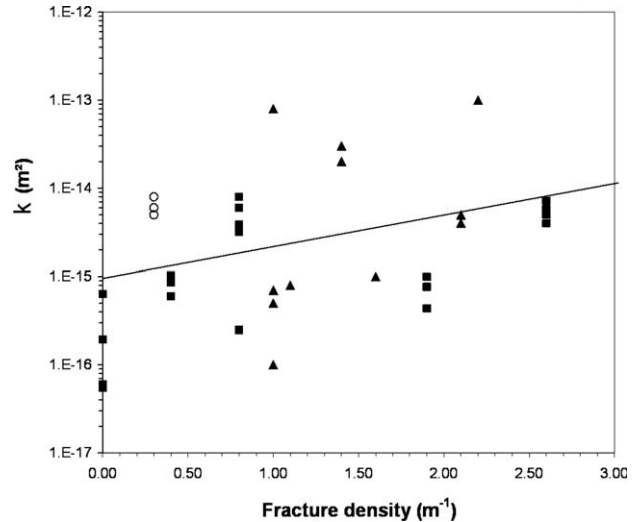


**Figure 6.** Permeability in the three cases as a function of fracture density in the tested interval. Data are for pneumatic injection tests in tunnel boreholes Perm (squares), surface boreholes SC (triangles) and chamber C (circles). The solid line is the best fit  $y = 9.54e^{0.824x}$  with a correlation coefficient  $R^2 = 0.14$

small decrease in air permeability, from  $1.5 \times 10^{-13}$  to  $1.0 \times 10^{-13} \text{ m}^2$ , can be seen between 4 and 8 February 2012, assuming that the air-filled porosity remains constant. Since differential barometric pressure monitoring reflects the natural conditions of the medium, especially in terms of water saturation, this decrease in air permeability would reveal a small increase in the water saturation of the rock. Available infiltration data and water drip rate measured at the roof of chamber C are currently not precise enough to identify such small changes in the medium. It is planned to use electric resistivity monitoring as a complementary tool for the monitoring of water saturation as in Daily *et al.* [1992].

## 7. Conclusion

[56] A thorough determination of pneumatic parameters in the field requires the acquisition and interpretation of many experimental data. Especially when dealing with heterogeneous fracture networks in variably saturated media, measurements must be repeated for various air flow rates, various locations and various hydrological conditions.

[57] Here we propose an integrated study of gas-phase flow parameters. Two experimental methods are used to determine air permeability, that can easily be implemented in the field, in a variety of settings and scales. In the Roselend Natural Laboratory, air permeability is investigated in deep and shallow boreholes, as well as in chamber C, by both pneumatic injection tests and differential barometric pressure monitoring.

[58] Experimental data are combined with numerical simulations to obtain both air permeability and air-filled porosity. Since each tested interval has its specific shape and boundary conditions, it is recommended to interpret the experimental data using 3-D numerical simulations. The widely used 1-D radial approximation leads to air

permeability values that differ on average of 30% from the 3-D simulations (from  $-54\%$  to  $+200\%$ ).

[59] The permeability values obtained here at different scales span four orders of magnitude, thus highlighting the strong heterogeneity of fractured rocks. In the chamber, a 1 order-of-magnitude difference is found between the air permeability values obtained from pneumatic injection tests and from differential barometric pressure monitoring. This discrepancy is interpreted as a scale effect resulting from the approximation of the heterogeneous fractured rock by a homogeneous numerical model. The difference between the rock volumes investigated by pneumatic injection tests and by differential barometric pressure monitoring may also play a role.

[60] The flow parameters obtained in this study will be used to interpret tracing experiments conducted at the Roselend Natural Laboratory with aqueous [Pili et al., 2008a] or gaseous tracers. They will also serve to design future tracing experiments at all scales.

[61] The isolated chamber C, one of the settings presented in this study, is a very useful tool which gives access to parameters on large scales, intermediate between the borehole and the regional scales. The experimental and numerical methods presented here for chamber C are also of interest in the design and validation of air- or water-tight bulkhead, especially for underground waste repositories [Martino et al., 2007].

[62] **Acknowledgments.** We thank Jean-Christophe Sabroux for fruitful discussions and Jérôme Wassermann for initiating air permeability measurements at the Roselend Natural Laboratory. The technical help of Patrick Carrera and Marc Perrier is greatly acknowledged. We thank Bertrand Menotto for the building of the air-tight bulkhead. Thanks go the city of Beaufort for giving access to the Roselend Natural Laboratory. We thank the editors and the three anonymous reviewers for their comments that greatly improved the manuscript. This is IPGP contribution number 3330.

## References

- Ahlers, C. F., S. Finsterle, and G. S. Bodvarsson (1999), Characterization and prediction of subsurface pneumatic response at Yucca Mountain, Nevada, *J. Contam. Hydrol.*, *38*(1–3), 47–68.
- Baehr, A. L., and M. F. Hult (1991), Evaluation of unsaturated zone air permeability through pneumatic tests, *Water Resour. Res.*, *27*(10), 2605–2617.
- Berkowitz, B. (2002), Characterizing flow and transport in fractured geological media: A review, *Adv. Water Resour.*, *25*(8–12), 861–884.
- Bogdanov, I., V. V. Mourzenko, J. F. Thovert, and P. M. Adler (2003), Effective permeability of fractured porous media in steady state flow, *Water Resour. Res.*, *39*(1), 1023–1039, doi:10.1029/2001WR000756.
- Bossart, P., P. M. Meier, A. Moeri, T. Trick, and J. C. Mayor (2002), Geological and hydraulic characterisation of the excavation disturbed zone in the Opalinus Clay of the Mont Terri Rock Laboratory, *Eng. Geol.*, *66*(1–2), 19–38.
- Brace, W. F. (1984), Permeability of crystalline rocks—New in situ measurements, *J. Geophys. Res.*, *89*(B6), 4327–4330.
- Clauser, C. (1992), Permeability of crystalline rocks, *EOS*, *73*(21), 233–240.
- Cook, P. J., R. Salve, B. M. Freifeld, and Y. T. Tsang (2003), Measurement system for systematic hydrological characterization of unsaturated fractured welded tuff in a mined underground tunnel, *Ground Water*, *41*(4), 449–457.
- Daily, W., A. Ramirez, D. Labrecque, and J. Nitao (1992), Electrical resistivity tomography of vadose zone water movement, *Water Resour. Res.*, *28*(5), 1429–1442.
- Freifeld, B. M. (2001), Estimation of fracture porosity in an unsaturated fractured welded tuff using gas tracer testing, Ph.D. thesis, Lawrence Berkeley Natl. Lab., Univ. of Calif., Berkeley.
- Guzman, A. G., A. M. Geddis, M. J. Henrich, C. F. Lohrstorfer, and S. P. Neuman (1996), Summary of air permeability data from single-hole injection tests in unsaturated fractured tuffs at the Apache Leap Research Site: Results of steady-state test interpretation, Rep. NUREG/CR-6360, Univ. of Arizona, Tuscon, Arizona.
- Hinds, J. J., G. S. Bodvarsson, and G. H. Nieder-Westermann (2003), Conceptual evaluation of the potential role of fractures in unsaturated processes at Yucca Mountain, *J. Contam. Hydrol.*, *62–63*, 111–132.
- Hirt, C. W. (1968), Heuristic stability theory for finite-difference equations, *J. Comput. Phys.*, *2*(4), 339–355.
- Hyun, Y., S. P. Neuman, V. V. Vesselinov, W. A. Illman, D. M. Tartakovsky, and V. Di Federico (2002), Theoretical interpretation of a pronounced permeability scale effect in unsaturated fractured tuff, *Water Resour. Res.*, *38*(6), 1092–1100.
- Illman, W. A. (2004), Analysis of permeability scaling within single boreholes, *Geophys. Res. Lett.*, *31*(5), L06503, doi:10.1029/2003GL019303.
- Illman, W. A. (2005), Type curve analyses of pneumatic single-hole tests in unsaturated fractured tuff: Direct evidence for a porosity scale effect, *Water Resour. Res.*, *41*(4), W0418, doi:10.1029/2004WR003703.
- Illman, W. A. (2006), Strong field evidence of directional permeability scale effect in fractured rock, *J. Hydrol.*, *319*(1–4), 227–236.
- Illman, W. A., and D. L. Hughson (2005), Stochastic simulations of steady state unsaturated flow in a three-layer, heterogeneous, dual continuum model of fractured rock, *J. Hydrol.*, *307*(1–4), 17–37.
- Illman, W. A., and S. P. Neuman (2000), Type-curve interpretation of multirate single-hole pneumatic injection tests in unsaturated fractured rock, *Ground Water*, *38*(6), 899–911.
- Illman, W. A., and S. P. Neuman (2001), Type curve interpretation of a cross-hole pneumatic injection test in unsaturated fractured tuff, *Water Resour. Res.*, *37*(3), 583–603, doi:10.1029/2000WR900273.
- Illman, W. A., and S. P. Neuman (2003), Steady-state analysis of cross-hole pneumatic injection tests in unsaturated fractured tuff, *J. Hydrol.*, *281*(1–2), 36–54.
- Illman, W. A., and D. M. Tartakovsky (2005), Asymptotic analysis of cross-hole pneumatic injection tests in unsaturated fractured tuff, *Adv. Water Resour.*, *28*(11), 1217–1222.
- Jakubick, A. T., and T. Franz (1993), Vacuum testing of the permeability of the excavation damaged zone, *Rock Mech. Rock Eng.*, *26*(2), 165–182.
- Kearl, P. M., R. J. Zinkl, J. J. Dexter, and T. Cronk (1990), Air permeability measurements of the unsaturated Bandelier Tuff near Los-Alamos, New-Mexico, *J. Hydrol.*, *117*(1–4), 225–240.
- Kim, H., Y. Lettry, D. Park, D. Ryu, B. Choi, and W. Song (2012), Field evaluation of permeability of concrete linings and rock masses around underground lined rock caverns by a novel in-situ measurement system, *Eng. Geol.*, *137–138*, 97–106.
- LeCain, G. (1997), Air-injection testing in vertical boreholes in welded and nonwelded tuff, Yucca Mountain, Nevada, Water-Resour. Investig. Rep. 96–4262, U.S. Geol. Surv., Denver, Colorado.
- Long, J. C. S., J. S. Remer, C. R. Wilson, and P. A. Witherspoon (1982), Porous-media equivalents for networks of discontinuous fractures, *Water Resour. Res.*, *18*(3), 645–658.
- Martino, J. B., D. A. Dixon, E. T. Kozak, M. Gascoyne, B. Vignal, Y. Sugita, T. Fujita, and Masumoto, K. (2007), The tunnel sealing experiment: An international study of full-scale seals, *Phys. Chem. Earth*, *32*(1–7), 93–107.
- Mourzenko, V. V., I. Bogdanov, J. F. Thovert, and P. M. Adler (2011), Three-dimensional numerical simulation of single-phase transient compressible flows and well-tests in fractured formations, *Math. Comput. Simul.*, *81*(10), 2270–2281.
- Neeper, D. A. (2002), Investigation of the vadose zone using barometric pressure cycles, *J. Contam. Hydrol.*, *54*(1–2), 59–80.
- Neuman, S. P. (1994), Generalized scaling of permeabilities—Validation and effect of support scale, *Geophysical Res. Lett.*, *21*(5), 349–352.
- Ni, C., and T. J. Yeh (2008), Stochastic inversion of pneumatic cross-hole tests and barometric pressure fluctuations in heterogeneous unsaturated formations, *Adv. Water Resour.*, *31*(12), 1708–1718.
- Oldenburg, C. M., J. L. Lewicki, L. Dobeck, and L. Spangler (2010), Modeling gas transport in the shallow subsurface during the ZERT CO<sub>2</sub> release test, *Transp. Porous Media*, *82*(1), 77–92.
- Patriarche, D., E. Pili, P. Adler, and J.-F. Thovert (2007), Stereological analysis of fractures in the Roselend tunnel and permeability determination, *Water Resour. Res.*, *43*, W09421, doi:10.1029/2006WR005471.
- Peyret, R., and T. D. Taylor (1985), *Computational Methods for Fluid Flow*, Springer, New York.

- Pili, E., F. Perrier, and P. Richon (2004), Dual porosity mechanism for transient groundwater and gas anomalies induced by external forcing, *Earth Planetary Sci. Lett.*, 227(3–4), 473–480.
- Pili, E., S. Bureau, F. Perrier, D. Patriarche, L. Charlet, P. M. Adler, and P. Richon (2008a), Reactive transport and residence times in unsaturated fractured rocks from field-scale experiments, In *Developments in Earth and Environmental Sciences*, volume 7, edited by M. O. Barnett, and D. B. Kent, pp. 441–468, Elsevier Science, Amsterdam.
- Pili, E., P. Richon, M. Moreira, P. Agrinier, J. C. Sabroux, and P. M. Adler (2008b), The ROSELEND-Gas Project: Research on sollicitation effects in a large-scale experiment under natural dynamics with gas, *EOS Trans. AGU*, 89(53), Fall Meet. Suppl., Abstract H53A-1000.
- Richon, P., F. Perrier, J. C. Sabroux, M. Trique, C. Ferry, V. Voisin, and E. Pili (2005), Spatial and time variations of radon-222 concentration in the atmospheres of a dead-end horizontal tunnel, *J. Environ. Radioactiv.*, 78(2), 179–198.
- Sethian, J. A., and P. Smereka (2003), Level set methods for fluid interfaces, *Annu. Rev. Fluid Mech.*, 35, 341–372.
- Sun, Y., and C. R. Carrigan (2012), Modeling noble gas transport and detection for the comprehensive nuclear-test-ban treaty, *Pure Appl. Geophys.*, 1–16.
- Switzer, C., and D. S. Kosson (2007), Evaluation of air permeability in layered unsaturated materials, *J. Contam. Hydrol.*, 90(3–4), 125–145.
- Unger, A., S. Finsterle, and G. Bodvarsson (2004), Transport of radon gas into a tunnel at Yucca Mountain—Estimating large-scale fractured tuff hydraulic properties and implications for the operation of the ventilation system, *J. Contam. Hydrol.*, 70(3–4), 153–171.
- Vesselinov, V. V., and S. P. Neuman (2001), Numerical inverse interpretation of single-hole pneumatic tests in unsaturated fractured tuff, *Ground Water*, 39(5), 685–695.
- Vesselinov, V. V., S. P. Neuman, and W. A. Illman (2001a), Three-dimensional numerical inversion of pneumatic cross-hole tests in unsaturated fractured tuff 1. Methodology and borehole effects, *Water Resour. Res.*, 37(12), 3001–3017.
- Vesselinov, V. V., S. P. Neuman, and W. A. Illman (2001b), Three-dimensional numerical inversion of pneumatic cross-hole tests in unsaturated fractured tuff 2. Equivalent parameters, high-resolution stochastic imaging and scale effects, *Water Resour. Res.*, 37(12), 3019–3041.
- Wang, J. S. Y., R. C. Trautz, P. J. Cook, S. Finsterle, A. L. James, and J. Birkholzer (1999), Field tests and model analyses of seepage into drift, *J. Contam. Hydrol.*, 38(1–3), 323–347.
- Wassermann, J., J. C. Sabroux, S. Pontreau, S. Bondiguel, S. Guillon, P. Richon, and E. Pili (2011), Characterization and monitoring of the excavation damaged zone in fractured gneisses of the Roselend tunnel, *French Alps, Tectonophysics*, 503(1–2), 155–164.
- Zhou, Q. L., H. H. Liu, G. S. Bodvarsson, and C. M. Oldenburg (2003), Flow and transport in unsaturated fractured rock: Effects of multiscale heterogeneity of hydrogeologic properties, *J. Contam. Hydrol.*, 60(1–2), 1–30.